# Chapter 5

# Angle-dependent reflectivity recovery

## 5.1 Introduction and overview

During the past decade, the use of AVO (amplitude variation with offset) analysis in petroleum exploration has become increasingly common. Even though the goal of AVO analysis is to observe the anomalous angle-dependent reflectivity behavior of a reflector, the name *amplitude variation with offset* was chosen because most of the amplitude analysis is done in the common midpoint domain.

To analyze the properties of the reflector correctly, we need to know the angle-dependent reflectivity, which is often called AVA (*amplitude variation with angle*). When a target reflector is close to horizontal, and velocity does not change much in the lateral direction, angle-dependent reflectivity can be obtained by measuring amplitudes along the offset, followed by ray tracing for each event to determine the corresponding incidence angle to the reflector. If a target reflector has a complex structure and strong lateral velocity variation, however, AVO may not be the same as AVA because the amplitude can be affected not only by the angle-dependent reflectivity but also by wave focusing or defocusing caused by propagation through complex velocities or structures. Resnick et al. (1987) discuss the fact that dips introduce serious problems for AVO analysis. They conclude that performing prestack migration on the data before doing AVO analysis is a necessity.

Most present-day seismic migration schemes determine only the reflection coefficient of the zero offset or averaged reflectivity over a range of reflection angles for each depth point in the subsurface. This is mainly due to a simplified imaging condition.

Recently, more correct methods for estimating angle-dependent reflectivity, based on migration algorithms, have been developed. De Bruin et al. (1990b) presented a method for estimating angle-dependent reflectivity using a scalar prestack $x-\omega$ migration scheme. First, the multicomponent data were decomposed into PP, PS, SP, and SS modes and each of them migrated separately. Tests with synthetic data showed that the method was able to retrieve the reflectivity function with considerable accuracy for horizontal layers, but when dip was present (de Bruin et al., 1990a), the retrieved function was incorrectly shifted (in angle) because of the assumption of a horizontally-layered earth which is implicit in their imaging principle (integration along constant Snell parameter traces). Another limitation of their method is that the estimated reflectivities do not correspond to the local reflectivities because the decomposition is carried out in the Fourier domain. Lumley and Beydoun (1991) introduced a different method for retrieving the reflectivity function, using an elastic, prestack Kirchhoff migration scheme. Their imaging principle was not limited by the horizontal layer assumption and was successfully applied to synthetic and real data. However, as a consequence of the Kirchhoff approach, their method suffers from the restrictions imposed by the ray approximation associated with the evaluation of the Green's function. Cunha Filho (1992) proposed the local plane-wave-response imaging after prestack reverse-time migration (McMechan, 1983) for the angle-dependent reflectivity recovery. This approach solves the spatial variability of the reflectivity by applying the imaging locally in the space domain instead of the imaging in the wavenumber domain. However, it requires very expensive elastic forward modelling and reverse-time migration.

Plane wave synthesis imaging is a promising alternative for the angle-dependent reflectivity recovery because it can be applied to any arbitrary structure and implicitly uses the spatially varying plane-wave-response imaging. In addition to that, the PWS imaging provides incidence-angle of the wavefront along the datum plane where the plane wave is synthesized.

This chapter describes the plane wave synthesis imaging as an tool for the angle-dependent reflectivity recovery. First I describe the forward model of a seismic shot record in detail. Then I explain how the plane wave synthesis imaging recovers the angle-dependent reflectivity. Then I show some examples of angle-dependent reflectivity recovery of each imaging method using synthetic data for comparison.

## 5.2 The forward model

Since reflectivity imaging is an inversion from seismic data collected at the surface, it is important to understand the implied forward model that relates the reflectivity to surface seismic data. The monochromatic forward model for a seismic shot record (chapter 2) can be written as follows:

$$\mathbf{g}_j(z_0) = F(z_0, z_0)\mathbf{s}_j(z_0), \tag{5.1}$$

with

$$F(z_0, z_0) = \sum_{n=1}^{N} W(z_0, z_n)R(z_n)W(z_n, z_0). \tag{5.2}$$

### 5.2.1 Propagation operators

If we want to model seismic data correctly, propagation operator $W$ should be a time extrapolation since wave fields extrapolate in time physically. However, the time extrapolation is not efficient in computation. Instead, depth extrapolation is widely used, which is efficient in computation. If we use depth extrapolation as a propagation operator, however, we cannot model the correct amplitude of the wave field because the energy of the wave field in a lossless medium is preserved in time, not in depth.

This does not mean that the amplitude of wave field obtained by depth extrapolation is totally incorrect because most of the energy recorded in reflection seismic travels near the vertical direction and the wave field becomes a plane wave in the far distance where the energy of the wave field is preserved both in time and depth. Therefore, if the source wave field is a plane wave, the amplitude of the wave field after depth extrapolation behaves similarly to that of the wave field obtained by time extrapolation.

### 5.2.2 Reflectivity matrix

The property of the angle-dependent reflectivity matrix $R(z_n)$ in equation (5.1) becomes clearer if we look at it in the Fourier domain as de Bruin et al. (1990) does. In order to obtain an expression for $R(k_x, z_n, \omega)$, we start with the well-known angle-dependent reflection coefficient $R(z_n, \alpha)$ for two acoustic half-spaces separated by an interface at $z_n$:

$$R(z_n; \alpha) = \frac{\rho_2 c_2 \cos\alpha - \rho_1\sqrt{c_1^2 - c_2^2 \sin^2\alpha}}{\rho_2 c_2 \cos\alpha + \rho_1\sqrt{c_1^2 - c_2^2 \sin^2\alpha}}, \tag{5.3}$$

where $c_1$ and $c_2$ are the velocities, $\rho_1$ and $\rho_2$ are the mass densities of the upper and lower half-space, respectively, and $\alpha$ is the angle of incidence. By substituting $k_1 = \omega/c_1$, $k_2 = \omega/c_2$, and $k_x = k_1 \sin\alpha$ into equation (5.3) we obtain

$$R(k_x, z_n, \omega) = \frac{\rho_2\sqrt{k_1^2 - k_x^2} - \rho_1\sqrt{k_2^2 - k_x^2}}{\rho_2\sqrt{k_1^2 - k_x^2} + \rho_1\sqrt{k_2^2 - k_x^2}}. \tag{5.4}$$

As an example, Figure 5.1 shows the angle-dependent reflection coefficients in the $(k_x, \omega)$ and $(x, \omega)$ domains when $c_1 = 1500m/s$, $c_2 = 3000m/s$, $\rho_1 = 1000kg/m^3$, and $\rho_2 = 1000kg/m^3$. Since the reflection is a convolution of the downgoing wave field with the reflection coefficient, the reflectivity matrix in equation (5.2) can be visualized by taking the reflection coefficient for a given frequency in Figure 5.1 and making a matrix whose columns are down-shifted reflection coefficients of each other. Figure 5.2 shows this reflectivity matrix when $\omega = \pi/4$.

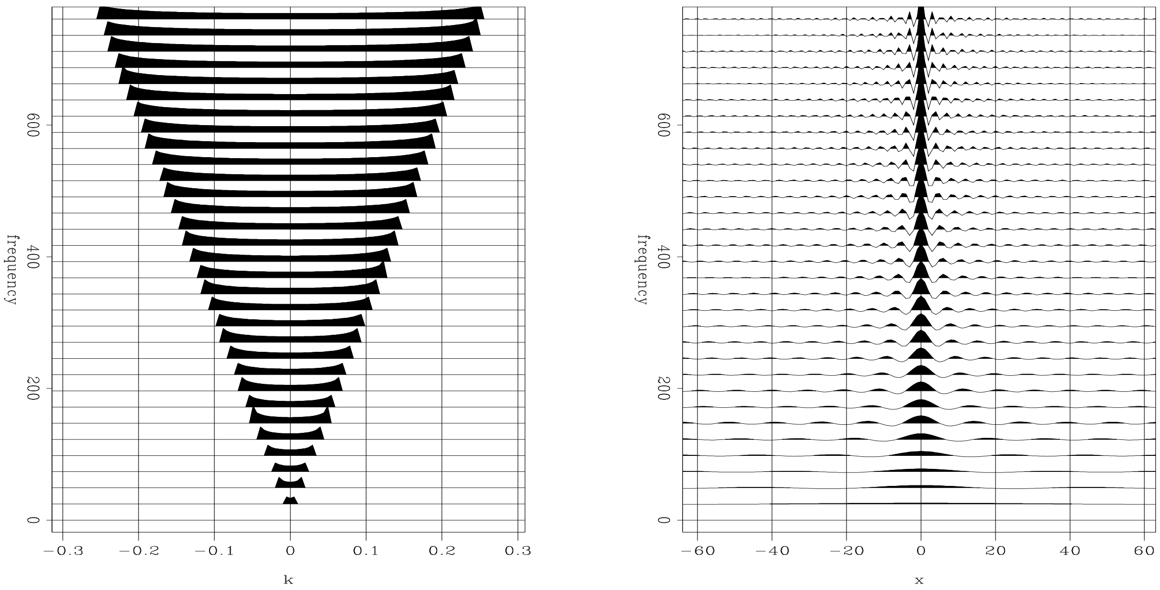


FIG. 5.1. Angle-dependent reflection coefficients in $(k_x, \omega)$ (left) and $(x, \omega)$ (right) domains when $c_1 = 1500m/s$, $c_2 = 3000m/s$,$\rho_1 = 1000kg/m^3$, and $\rho_2 = 1000kg/m^3$. ava-rc-wk-wx [R]

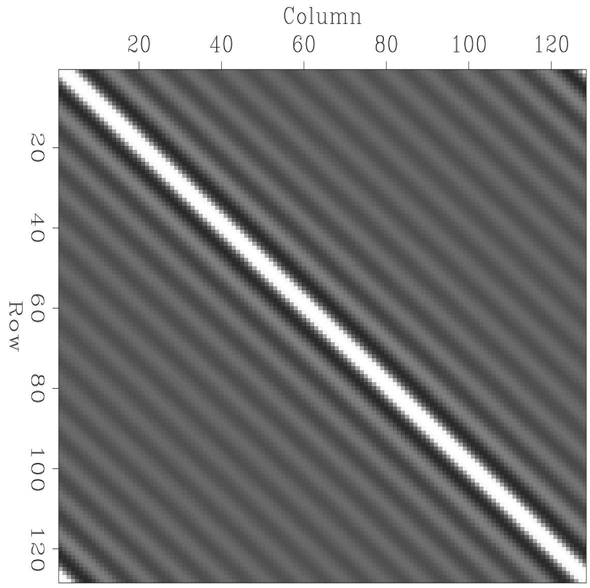


FIG. 5.2. Reflectivity matrix $R$ for $\omega = \pi/4$. ava-rc-mat [R]

## 5.3 Wave field extrapolation into subsurface

In prestack imaging, the first step is the extrapolation of the source and received wave fields into subsurface. The source and received wave fields are extrapolated recursively for each depth level as follows:

$$\mathbf{s}(z_n) = W(z_n, z_m)\mathbf{s}(z_m) \tag{5.5}$$

and

$$\mathbf{g}(z_n) = W^*(z_n, z_m)\mathbf{g}(z_m), \tag{5.6}$$

where $*$ denotes the adjoint and implies that the received wave field is extrapolated backward in time. By substituting equations (5.5) and (5.6) into the forward model (equation (5.1)), we have

$$\mathbf{g}(z_n) = W^*(z_n, z_0)W(z_0, z_n)R(z_n)W(z_n, z_0)\mathbf{s}(z_0). \tag{5.7}$$

If we assume that the extrapolation operator $W$ is a unitary operator, equation (5.7) becomes

$$\mathbf{g}(z_n) = R(z_n)\mathbf{s}(z_n). \tag{5.8}$$

Then using the above relation, we perform the imaging to retrieve reflectivity matrix $R(z_n)$ from $\mathbf{g}(z_n)$ and $\mathbf{s}(z_n)$ for each depth level.

Therefore, one of the most important properties of the extrapolation operator is the unitary that makes equation (5.8) valid. Even though many algorithms based on the wave equation are accepted as unitary operators, each algorithm has a different property in terms of closeness to unitary. Among the many extrapolation algorithms which allows lateral velocity changes like finite-difference (Claerbout, 1985), PSPI (Gazdag and Sguazzero, 1984) and split-step Fourier (Stoffa and Fokkema, 1990). I chose the split-step Fourier method (Stoffa and Fokkema, 1990) for this thesis because of its pseudounitary property (Appendix A).

To show the closeness to unitary of the split-step Fourier extrapolation, I tested a plane wave extrapolation followed by its adjoint operator in the Marmousi velocity model. The input is a plane wave which is horizontally aligned spikes at time equals zero (Figure 5.3(a)). Figure 5.3(b) shows synthesis operator obtained by extrapolating a plane wave from depth level 800 m to surface. Figure 5.3(c) shows source wave field obtained by applying its adjoint operator to the synthesis operator which is extrapolating the synthesis operator at surface to depth level 800 m. Figure 5.4 is amplitude of the source wave field (Figure 5.3(c)) along the plane wave.

## 5.4 Imaging conditions

### 5.4.1 Conventional prestack imaging

In conventional prestack imaging as in shot profile imaging (Claerbout, 1985), the reflectivity is obtained by deconvolving the downgoing wave field from the upcoming wave field in the $(x, \omega)$ domain as follows:

$$X(x, z_n, \omega) = \frac{\mathbf{g}(x, z_n, \omega)\mathbf{s}^*(x, z_n, \omega)}{\mathbf{s}(x, z_n, \omega)\mathbf{s}^*(x, z_n, \omega) + \epsilon^2}, \tag{5.9}$$

where $\epsilon^2$ represents a small positive value introduced for stability because $\mathbf{s}(x, z_n, \omega)$ may contain zeros. Then imaging is carried out by summation over all frequencies to extract the zero-time component of the reflectivity as follows:

$$\mathbf{r}(x, z_n) = \sum_{\omega} X(x, z_n, \omega). \tag{5.10}$$

Therefore we obtain one reflection coefficient value for each point of the subsurface.

Since we performed the deconvolution in the $(x, \omega)$ domain by dividing the source wave from received wave in equation (5.9), we implicitly assumed the reflectivity matrix $R$ is

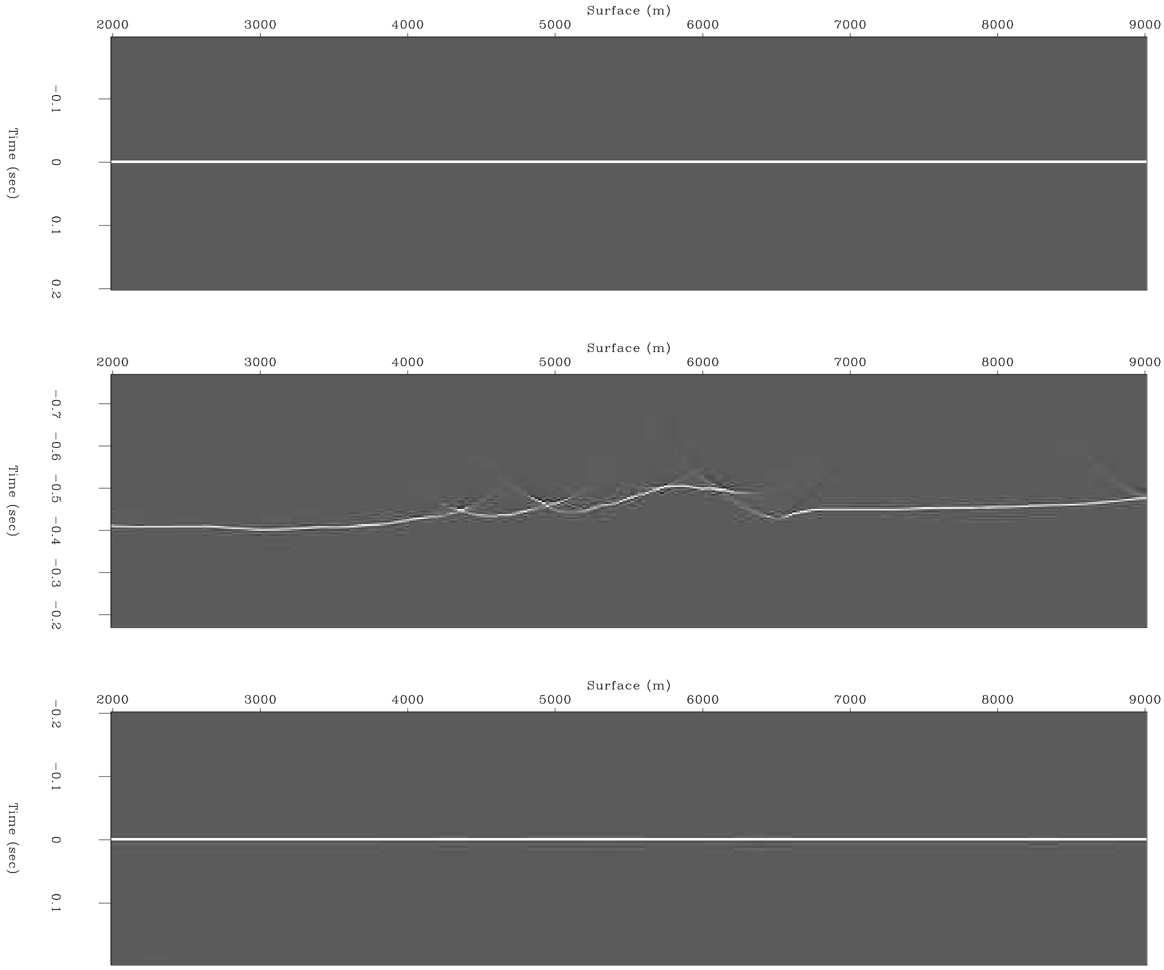


FIG. 5.3. Unitary property of the Split-step Fourier method. Top : Input plane wave ( $\mathbf{s}(z_n)$. Middle : Synthesis operator $\mathbf{s}(z_0) = W^*(z_0, z_n)\mathbf{s}(z_n)$. Bottom : source wave field at the datum $\tilde{\mathbf{s}}(z_n) = W(z_n, z_0)W^*(z_0, z_n)\mathbf{s}(z_n)$. $\boxed{\text{ava-unitary}}$ [CR]

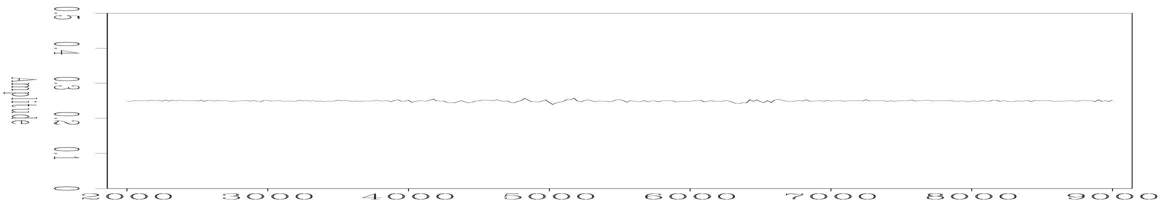


FIG. 5.4. Amplitude of source wave field at datum level. $\boxed{\text{ava-unitary-amp}}$ [CR]

a diagonal matrix. The diagonality of the reflectivity matrix $R$ implies locally reacting reflection coefficient. If we assume that source wave field acts like a planewave locally at reflector, the imaging condition used in the profile imaging will produce the reflection coefficient of the angle that corresponds to the local incidence angle of the source wave field at each point of the subsurface.

### 5.4.2 de Bruin's imaging condition

In order to retrieve the full reflectivity matrix, de Bruin et al. (1990) proposes another imaging condition (Figure 5.5). Instead of deconvolving in the spatial domain, they deconvolve in the Fourier domain $(k_x, \omega)$ after Fourier transforming both downgoing and upcoming waves, as follows:

$$X(k_x, z_n, \omega) = \frac{\mathbf{g}(k_x, z_n, \omega)\mathbf{s}^*(k_x, z_n, \omega)}{\mathbf{s}(k_x, z_n, \omega)\mathbf{s}^*(k_x, z_n, \omega) + \epsilon^2}. \tag{5.11}$$

The next step is to transform $X(k_x, z_n, \omega)$ into $X(p, z_n, \omega)$ by replacing the wavenumber $k_x$ with the ray parameter $p = k_x/\omega$. Then imaging is carried out in the $p - \omega$ domain along the lines of the constant $p$:

$$\mathbf{r}(p, z_n) = \sum_{\omega} X(p, z_n, \omega). \tag{5.12}$$

This imaging condition retrieve the full angle-dependent reflectivity. However, since the deconvolution is performed in the Fourier domain, it implies a spatially invariant reflectivity, which is the case of horizontal reflector in constant velocity medium. Thus it has the disadvantage that is of being difficult to implement a realistic model.

### 5.4.3 Imaging condition in plane wave synthesis imaging

In plane wave synthesis imaging, the deconvolution of the downgoing wave field from the upcoming wave field is performed in the same domain as profile imaging is (Figure 5.6). As explained in an earlier section, the deconvolution in the space domain implies diagonality of reflectivity matrix and the diagonal property is valid only if the source wave acts like a plane wave locally. This is the case of plane wave synthesis imaging because it synthesizes a plane wave source along the reflector before migration.

Therefore, in plane wave synthesis migration, we retrieve the angle-dependent reflectivity by using a conventional imaging condition.

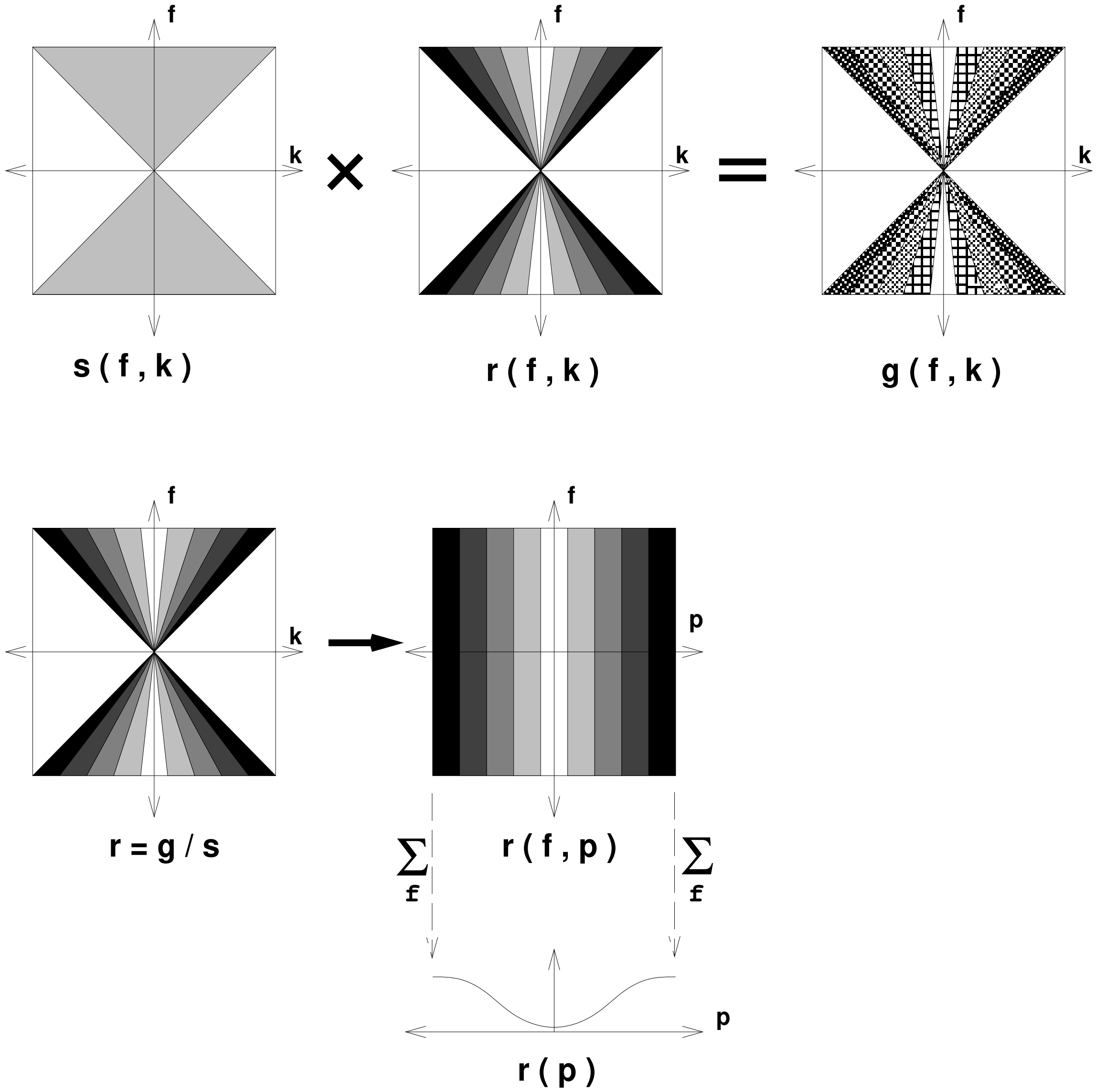


FIG. 5.5. Schematic representation of de Bruin's imaging condition $\boxed{\text{ava-fk-img}}$ [NR]

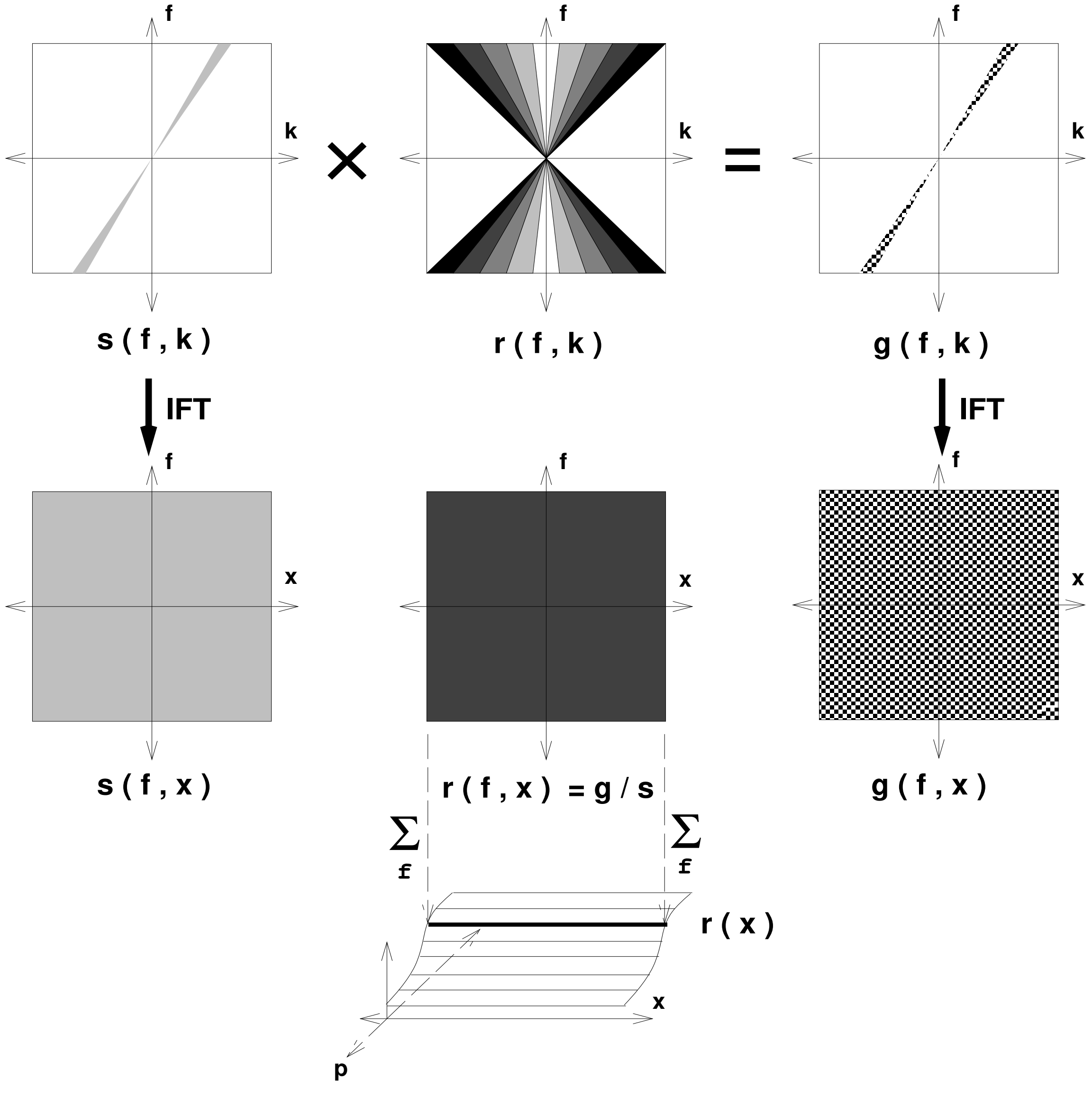


FIG. 5.6. Schematic representation of PWS imaging condition ava-fx-img [NR]

## 5.5 Examples

For the purposes of the comparison, let us consider the simple acoustic subsurface model shown in Figure 5.7a. Figure 5.7b displays the simulated seismic response of one shot record and shows the AVO effect clearly.

To obtain the angle-dependent reflectivity with conventional prestack imaging, I applied shot profile imaging with phase-shift extrapolation, acquired the offset-dependent reflectivity image (Figure 5.8a), and transformed it to an angle-dependent reflectivity image (Figure 5.8b) using the incidence angle at each depth location. Figure 5.9 shows an angle-dependent reflectivity image obtained using de Bruin's imaging condition and Figure 5.10, one obtained using plane wave synthesis imaging. All of them retrieve the general amplitude's increasing pattern with respect to the incidence angle.

To see the amplitude more clearly, I picked the amplitude of each reflectivity image at the reflector depth and plotted the amplitude as a function of the incidence angles (Figure 5.11). The comparison shows that the reflectivity obtained by the plane wave synthesis is closer to the theoretical solution.

For a more realistic example, the Marmousi dataset was tested. Figure 5.12 shows the image cube obtained by performing thirty-one constant incidence-angle PWS imaging and each constant incidence-angle image is obtained by patching twenty-one images obtained by synthesizing plane waves at twenty-one equi-spaced depth levels. The information of angle-dependent reflectivity is contained in the prestack image cube. To examine the angle-dependent reflectivity, four locations are selected and shown with theoretical angle-dependent reflectivities in Figures 5.13, 5.14, 5.15, and 5.16. We can see that the amplitude variations with angle in the images are very close to those of the theoretical reflectivity.

## 5.6 Summary

Although the imaging condition in plane wave synthesis imaging is equivalent to that of conventional profile imaging, plane wave synthesis imaging recovers full reflectivity matrix as de Bruin's imaging condition. This is achieved because of the property of the source wave field synthesized. Thus plane wave synthesis imaging is a promising method for recovering angle-dependent reflectivity for a nonflat reflector when lateral velocity changes. A test of a simple synthetic data showed that plane wave synthesis imaging among three

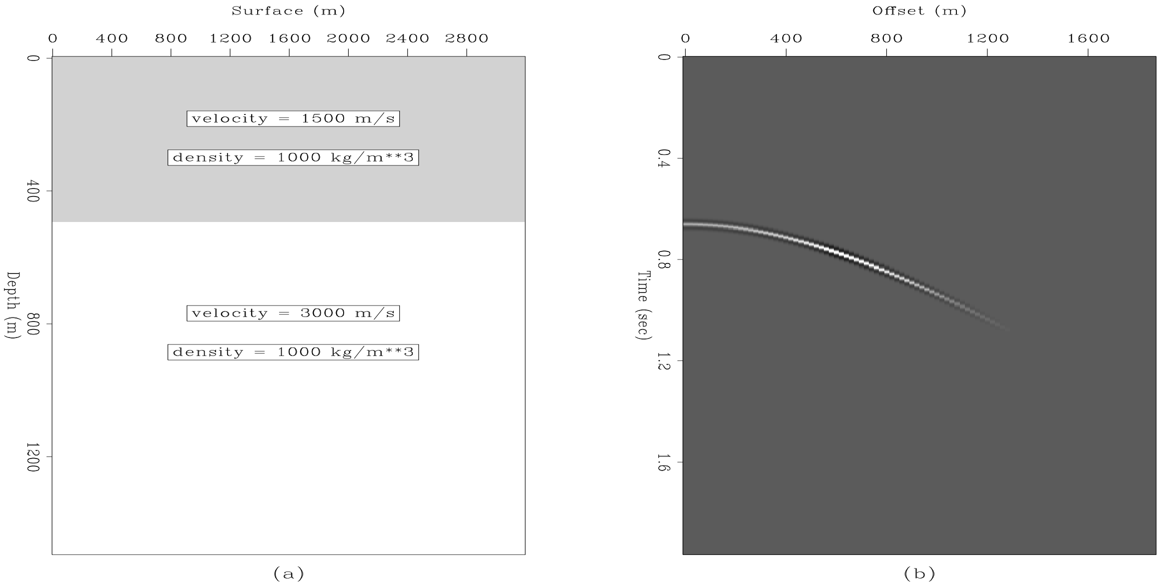


FIG. 5.7. (a): Subsurface model of a horizontally layered acoustic medium, containing one reflector at depth $z = 500m$. (b): Simulated seismic response from the acoustic model. ava-modl-shot [R]

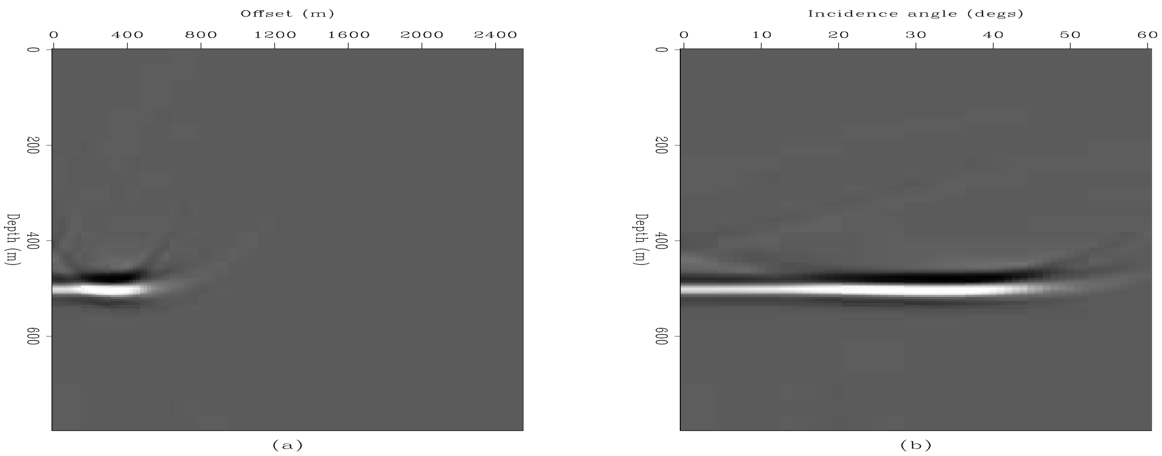


FIG. 5.8. Offset-dependent (a) and angle-dependent (b) reflectivity image obtained by profile imaging with the conventional imaging condition. ava-prf-img [CR]

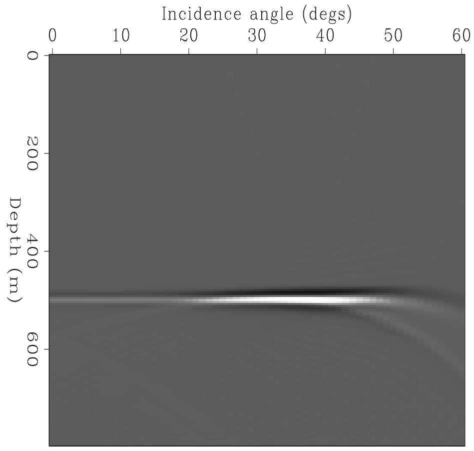


FIG. 5.9. Angle-dependent reflectivity image obtained by profile imaging with de Bruin's imaging condition. ava-prf-db-img [CR]

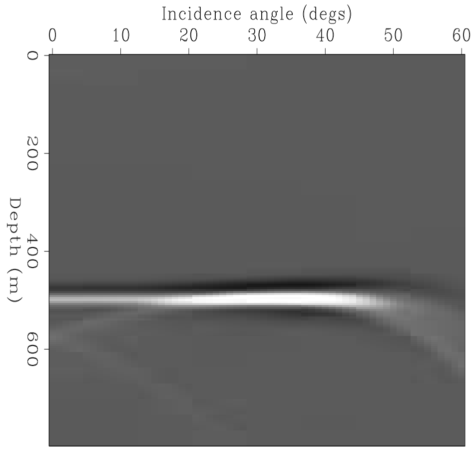


FIG. 5.10. Angle-dependent reflectivity image obtained by the plane wave synthesis imaging. ava-pws-img [CR]

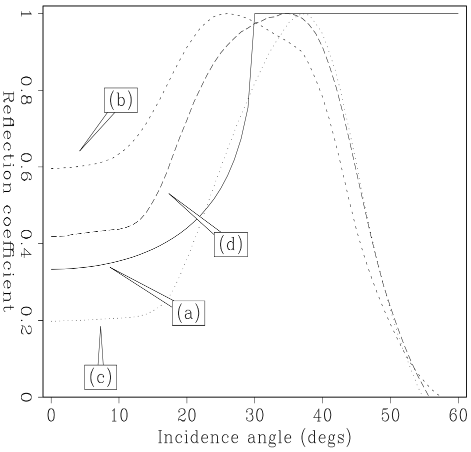


FIG. 5.11. Angle-dependent reflection coefficient as a function of the angle of incidence: (a) the theoretical result, (b) the result of profile imaging with conventional imaging condition, (c) the result of profile imaging with de Bruin's imaging condition, and (d) the result of plane wave synthesis imaging. ava-ava [CR]

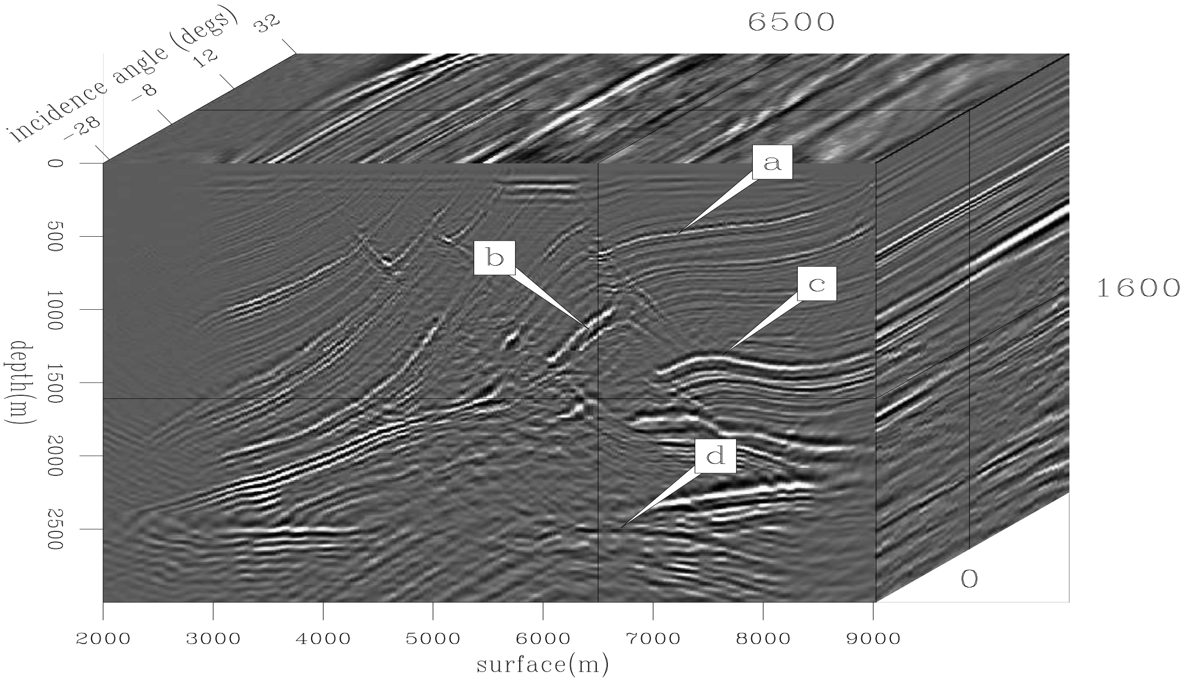


FIG. 5.12. Marmousi image obtained by PWS imaging. After angle-dependent reflectivity recovery, four locations, (a),(b),(c), and (d), were chosen to compare with theoretical angle-dependent reflectivity. ava-pws-all-marint-ava [CR]

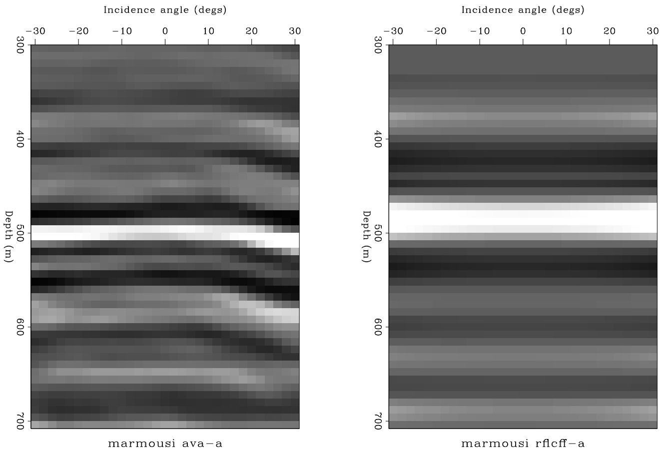


FIG. 5.13. Angle-dependent reflectivity obtained by PWS imaging (left) and theoretical reflectivity (right) for location (a). ava-marm-ava-rfl-com-1 [CR]

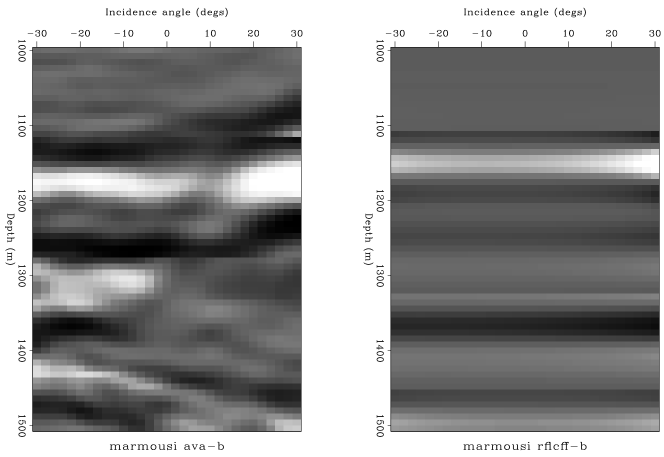


FIG. 5.14. Angle-dependent reflectivity obtained by PWS imaging (left) and theoretical reflectivity (right) for location (b). ava-marm-ava-rfl-com-2 [CR]

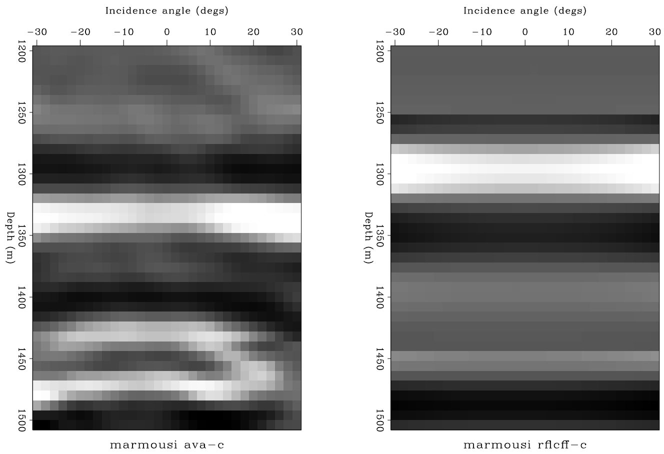


FIG. 5.15. Angle-dependent reflectivity obtained by PWS imaging (left) and theoretical reflectivity (right) for location (c). ava-marm-ava-rfl-com-3 [CR]

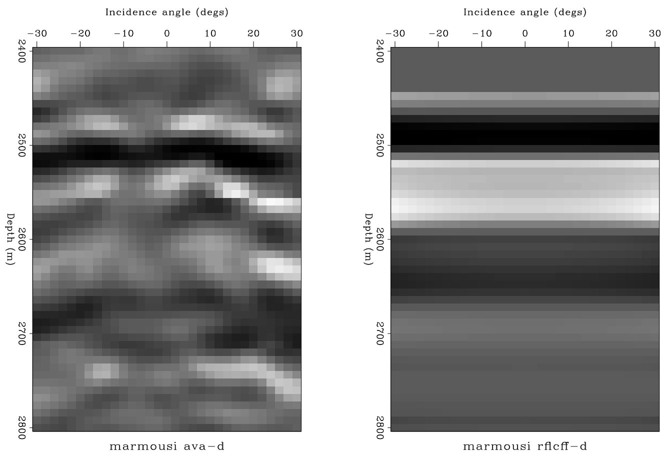


FIG. 5.16. Angle-dependent reflectivity obtained by PWS imaging (left) and theoretical reflectivity (right) for location (d). ava-marm-ava-rfl-com-4 [CR]

imaging techniques provide the closest result to the theoretical solution.